In-situ alloyed CoCrFeMnNi high entropy alloy

Chen, Peng; Yao, Xiyu; Attallah, Moataz M.; Yan, Ming

DOI:
10.1016/j.jmst.2021.11.083

Document Version
Peer reviewed version

Citation for published version (Harvard):
Chen, P, Yao, X, Attallah, MM & Yan, M 2022, 'In-situ alloyed CoCrFeMnNi high entropy alloy: microstructural development in laser powder bed fusion', *Journal of Materials Science & Technology*, vol. 123, pp. 123-135. https://doi.org/10.1016/j.jmst.2021.11.083

In-situ Alloyed CoCrFeMnNi High Entropy Alloy: Microstructural Development in Laser Powder Bed Fusion

Peng Chen[a,b], Xiyu Yao[a], Moataz M. Attallah[b,*], Ming Yan[a,*]

[a] *Department of Materials Science and Engineering, Southern University of Science and Technology, Shenzhen 518055, China*

[b] *Advanced Materials Processing Laboratory, University of Birmingham, Birmingham B15 2TT, UK*

* Corresponding authors: M.M.Attallah@bham.ac.uk, and yanm@sustech.edu.cn

Abstract: In-situ alloying has the potential to combine compositional flexibility of high entropy alloys (HEAs) and advanced forming capability of laser powder bed fusion (LPBF). This study fundamentally investigated the elemental homogenisation and grain development in the in-situ alloying process of a CoCrFeMnNi HEA, by investigating the basic units, the tracks and layers, and introducing Mn as an alloying element to the base CoCrFeNi HEA. Different modelling methods were employed to predict meltpool dimensions, and the results indicated the dependence of the modelling on practical meltpool modes. Delimitation of elemental distribution was found in keyhole meltpools since an intensive flow was generated due to recoil pressure. The homogeneity of in-situ alloyed Mn in single tracks was insufficient whether operated in conduction mode or keyhole mode, which required remelting from adjacent tracks and following layers to promote homogenisation significantly. The preferred orientation in single tracks along scanning directions changed from <001> to <101> as the scanning speed increased, although the cross-sections were similar in size at the same linear energy density. Such preference can be inherited during the printing process and lead to different textures in three-layer samples. It was also observed that applying hatch spacing smaller than a half meltpool width could coarsen the grains in a layer. Results from this study provide structure-parameter correlations for future microstructural tailoring and manipulation.

Keywords: Laser powder bed fusion, high entropy alloy, in-situ alloying, single track, elemental homogenisation

1. Introduction

In the past few years, CoCrFeNi-based high entropy alloys (HEAs), in particular CoCrFeMnNi, have drawn great attention due to their excellent mechanical performance. Their processing via additive manufacturing (AM) & 3D printing has been widely studied as well [1-7]. So far, the CoCrFeMnNi HEA has shown outstanding printability via laser powder bed fusion (LPBF) [8-11]. Its excellent printability also allows researchers to further explore the possibility in terms of compositional flexibility for promoting performance and applications. Approaches such as introducing a small amount of carbides or TiN nanoparticles to the HEA have led to improved mechanical properties [12-14]. However, LPBF may not be an ideal technique from HEA developing perspective if only pre-alloyed powder is going to be used, since for HEAs the chemical adjustment can be on a scale of 5-35 at. %, while the preparation of pre-alloyed powders for LPBF is often expensive and time-consuming [15-17]. For rapid prototyping of HEAs, in-situ alloying using blended powder has the potential to combine both the compositional flexibility of HEAs and the advanced forming capability of LPBF that originates from high-power laser.

The feasibility of in-situ alloying via LPBF has been assessed for conventional alloy systems, including Fe-Ni alloys, Ni superalloys, and Ti-based alloys [18-22]. It has been pointed out that elemental homogenisation could be a main challenge for LPBF in-situ alloying apart from densification. For HEAs with equiatomic compositions, the homogenisation of alloying elements can be even more challenging [23]. In a previous study on an in-situ alloyed HEA, a blend of pre-alloyed CoCrFeNi powder and elemental Mn powder has shown good printability [24]. Like other studies, however, only bulk samples were analysed and the homogenisation of in-situ alloyed was simply attributed to volumetric energy density. Single-track morphology has been correlated with printing quality to predict possible processing window [25-27]. Details involved in the track-to-track and layer-to-layer in-situ alloying processes have not been investigated yet, which actually can be important in order to

fully understand the in-situ alloying process, including associated microstructural development and elemental homogenisation.

This study aims to trace the LPBF in-situ alloying process back to its most fundamental units, single tracks. Figure 1 illustrates the logic and focus of this study. Meltpool dimensions, widths, and depths of cross-sections will be measured from single tracks scanned with and without Mn elemental powder to evaluate the influences of introducing secondary powder. Along with measured results, modelling methods will be employed to predict the dimensions of the meltpools and verify operating modes [28-30]. Elemental homogenisation and grain development will be compared in single tracks fabricated with different parameters. Since the LPBF process is not a simple pile of individual tracks, the inter-track and inter-layer remelting will be investigated as well through single-layer and three-layer experiments, respectively. In terms of printing parameters, laser power (P) and scanning speed (v) are directly responsible for energy input; hatch spacing (h) is another focal factor as it determines the remelting efficiency in each layer. They will be thoroughly examined. Elemental homogenisation and grain development in the LPBF in-situ alloying process will be characterised in the plane perpendicular to scanning directions, parallel to the cross-section of single tracks.

Results of this work demonstrated the applicability of representative modelling methods for conduction or keyhole modes. Mn homogenisation in different stages was revealed; its correlations with volumetric energy density were further analysed in terms of meltpool modes and scanning routes. For meltpool fabricated using different parameters but with similar cross-sections, their preferred crystalline orientations and grain growth were detailed. Based on the results, a fundamental understanding of the microstructural development in LPBF in-situ alloying is presented. Comprehending the mechanism of in-situ homogenisation and meltpool evolution can also help advance LPBF processes using different feedstocks.

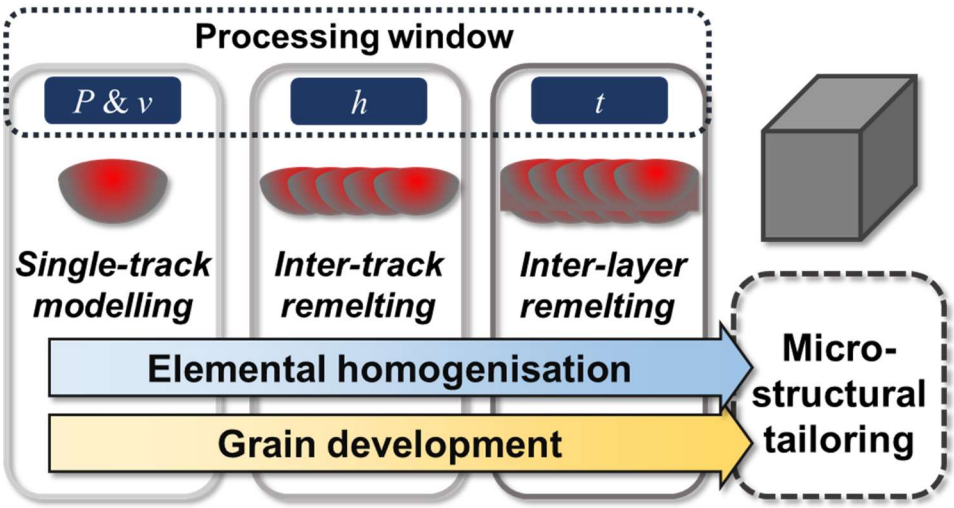

Figure 1. A schematic of the study route.

2. Material and methods

2.1. Sample preparation

Pre-alloyed CoCrFeNi powder was produced by Zhongyuan Advanced Materials and via gas atomisation. The pre-alloyed powder was overall spherical (Figure 2(a)) and with Dv50 of 21.5 μm. Elemental Mn powder (99.9% purity) was produced by Aladdin and in irregular shape (Figure 2(b)). The powders were firstly sieved by a 73-μm sieve, then weighed for quasi-equiatomic composition, and finally mixed by a WAB Turbula T2F mixer for 4 h. The blended powder is shown in Figure 2(c), and its composition is listed in Table 1. LPBF experiments were carried out on an SLM125HL (SLM Solutions) with argon protection. The laser diameter of the machine was ~67 μm. The layer thickness (t) and substrate temperature (T_0) were set as 30 μm and 100 °C (373 K) in all experiments. Before fabricating in-situ alloyed samples, at least 7 layers of pre-alloyed CoCrFeNi powder were scanned on a 316L substrate to ensure recoating quality and avoid contamination from the substrate material. The blended powder was then spread on the top of pre-alloyed beds for in-situ alloying experiments. A simple scanning strategy was employed with 90 ° rotation between adjacent layers, as shown by Figure

2(e). In the figure, building direction, transverse direction, and scanning direction were noted as BD, TD, and SD, respectively in this study. Since the processing window for in-situ alloying of CoCrFeMnNi HEA has been explored by a previous study [24], laser power and scanning speed for single-track experiments were selected closely to those parameters, while parameters for single-layer and three-layer experiments are listed in Table 2. Identical single-track experiments using the pre-alloyed CoCrFeNi powder were conducted as well to demonstrate the influences of additional Mn powder. were Laser parameters including laser power and scanning speed are noted as "*P* & *v*" to mark samples.

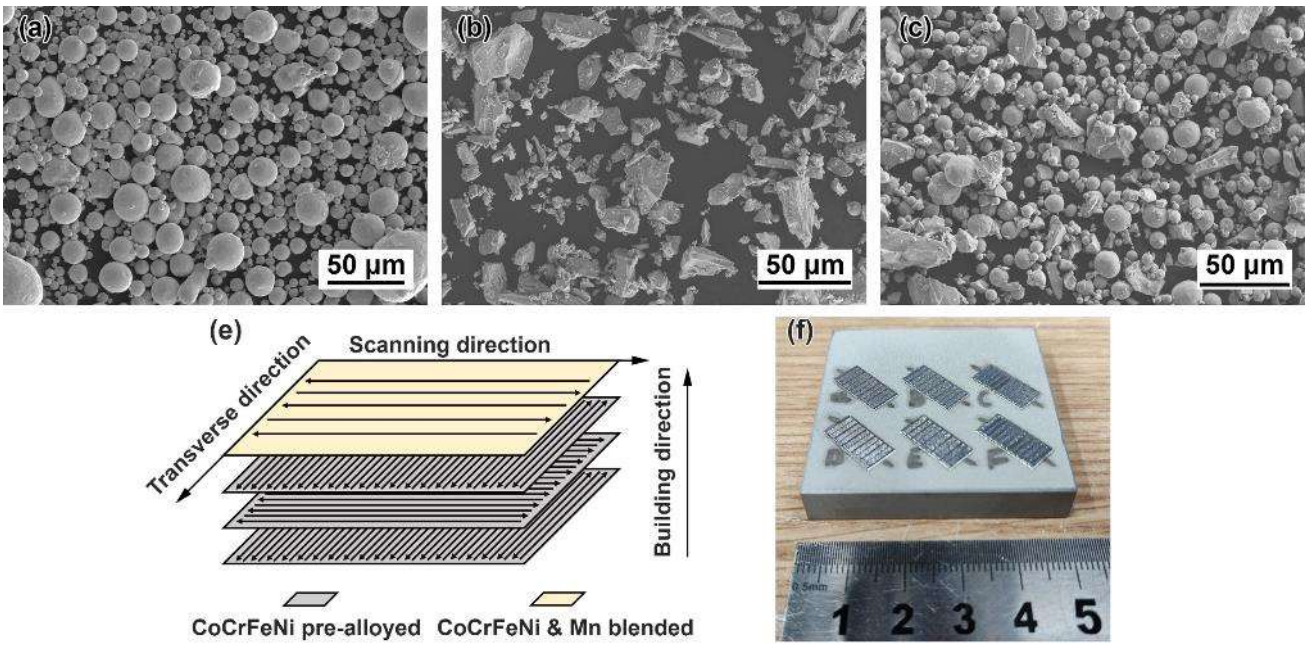

Figure 2. SEM images of (a) CoCrFeNi pre-alloyed powder, (b) Mn elemental powder, and (c) the blended powder. (e) An illustration of the scanning strategy for pre-alloyed beds and in-situ alloyed samples, and (f) a 316L substrate holding six pre-alloyed beds with as-built samples.

Table 1. Composition of the blended powder used in this study.

	Co	Cr	Fe	Ni	Mn

Blended powder	wt. %			79 (pre-alloyed)		21 (elemental)
	at. %	18.8	20.1	20.4	19.3	21.4

Table 2. Printing parameters for in-situ alloyed samples.

	Power, P (W)	Scanning speed, v (mm/s)	Hatch spacing, h (μm)
Single-track	150, 200, 250, 300	600, 700, 800, 900, 1000	/
Single-layer	150, 300	600, 1000	60, 70, 80, 90, 100
Three-layer	150, 200, 250, 300	600, 700, 800, 900, 1000	60, 100

2.2. Characterisation

Figure 2(f) shows as-built single tracks and single layers on a substrate. As-built samples were cut transversely to the scanning direction by electrical discharge machine (EDM). The cross-sections of samples were then ground and finished by a Buehler VibroMeting 2 Vibratory Polisher. To reveal meltpool structures, polished samples were electrochemically etched in a 10% oxalic acid solution for 100 s and at 2.5 V. A Leica DM2700 optical microscope (OM) was employed for the observation and measurement of meltpools. Depth (D) and width (W) results of meltpools were measured from 5 cross-sections, and the average was used. A Zeiss Merlin field emission scanning electron microscope (SEM) equipped with an energy dispersive spectrometer (EDS) and an electron back scattered diffraction (EBSD) system was employed for microstructural characterisation, including elemental distribution and grain structure determination.

2.3. Single-track modelling

Predicting the dimensions of LPBFed meltpools through modelling is essential for processing optimisation. Based on the laser parameters in single-track experiments, representative modelling

approaches from reports [28-30] were employed to calculate the width and depth of meltpools. Modelling approaches can also help assess the influences of adding elemental Mn powder to the meltpools.

Tang et al. [30, 31] introduced a method that presents an ideal meltpool shape based on the Rosenthal equation. The cross-section of meltpools is hypothesised to be semi-circle. The depth therefore equals half of the meltpool width, as follows:

$$D = \frac{W}{2} = \sqrt{\frac{2AP}{e\pi\rho C(T_m - T_0)v}} \tag{1}$$

where

A is the laser absorptivity,

ρ is the density (kg/m^3),

C is the thermal capacity (J/(kg*K)),

T_m is the melting temperature (K), and

T_0 is the substrate temperature (K) .

Rubenchik et al. [29, 32] provided scaling laws based on the Eagar-Tsai thermal model, which further modified the point heat source in the Rosenthal equation into a Gaussian heat distribution. Universal functions of B and p are used to describe normalised meltpool dimensions independent of materials and machines. The parameters are based on the normalised enthalpy introduced by Hann et al. [33], and defined by:

$$B = \frac{AP}{\pi^{1.5}\sqrt{avr^3}} \tag{2}$$

$$p = \frac{a}{vr} \tag{3}$$

where a stands for heat diffusivity (m^2/s). The algebraic expressions of depth D (B, p) and width

$W(B, p)$ are further shown as follows:

$$D(B, p) = \frac{r}{\sqrt{p}}\begin{bmatrix} 0.008 - 0.0048B - 0.047p - 0.099Bp \\ +(0.32 + 0.015B)p\ln p \\ +\ln B\,(0.0056 - 0.89p + 0.29p\ln p) \end{bmatrix} \quad (4)$$

$$W(B, p) = \frac{r}{Bp^3}\begin{bmatrix} 0.0021 - 0.047p + 0.34p^2 - 1.9p^3 - 0.33p^4 \\ +B(0.00066 - 0.007p - 0.00059p^2 + 2.8p^3 - 0.12p^4) \\ +B^2(-0.0007 + 0.15p - 0.12p^2 + 0.59p^3 - 0.023p^4) \\ +B^3(0.00001 - 0.00022p + 0.002p^2 - 0.0085p^3 + 0.0014p^4) \end{bmatrix} \quad (5)$$

Both methods from Tang et al. and Rubenchik et al. [29, 30] describe a meltpool fulfilled by molten materials. Meanwhile, the temperature at meltpool surface centre can be much higher than the boiling temperature of the material. Therefore, the meltpool expansion is consistently driven by heat conduction despite the possible vaporisation of the material. Their methods are hence noted as conduction-based ones in this study.

Fabbro et al. [34] introduced a method specifically for keyhole meltpools. The structure of keyhole meltpools includes an open cavity depressed by recoil pressure since the material vaporises at excessive temperature. Hence its development is distinct from the conduction meltpool mentioned above [28, 34]. This approach provides an expression of the aspect ratio $R=D/W$, as written below:

$$R = \frac{R_0}{1 + \frac{v}{V_0}} \quad (6)$$

with

$$R_0 = \frac{AP}{n2rK(T_b - T_0)} \quad (7)$$

$$V_0 = \frac{n}{m}\frac{a}{r} \quad (8)$$

where

K is the thermal conductivity (W/(m*K)),

T_b is the boiling temperature (K).

The parameters, m and n, are correlated to the Pélect number ($Pé=vr/a$) for given printing parameters. In this study, the $Pé$ ranges between $3.6 < Pe < 6.1$; m and n are set as 5 and 4, respectively [28].

To calculate meltpool dimensions, the involved physical properties of the CoCrFeNi HEA are provided in Table 3. Neglecting the temperature dependence of physical properties is one of the simplifications to maintain solvability. There have been other simplifications in the methods mentioned above, e.g., the influences of the powder layer, melt flows, and phase change have not been considered. Nevertheless, the applicability of the simplified models has been demonstrated in research on Al alloy, 316L SS, and Inconel 718 [35-37]. Their applicability will be further investigated by comparison with the measured data obtained from single-track experiments in this study.

Table 3. Physical properties of CoCrFeNi HEA

ρ (g/cm^3)	C (J/(kg*K))	K (W/(m*K))	T_m (K)	T_b (K)	A
8.16	444 [1]	21 [38]	1687 [1]	3070*	0.3, 0.6 [39, 40]

* The boiling point is calculated according to the rule of mixtures [41].

3. Results

3.1. Meltpool morphology

Figure 3 provides cross-section images of in-situ alloyed meltpools that formed using different process parameters. For each laser setting, two adjacent tracks are included. As the linear energy density (LED, defined by P/v [42]) increases, meltpools enlarge significantly. To further illustrate the dimensions of meltpools, measured depths of pre-alloyed and in-situ alloyed meltpools are plotted in Figure 4(a) and (b), respectively. The minimum depth of pre-alloyed and in-situ alloyed meltpools are both 60 μm at

the lowest *LED* of 0.15 J/mm. Despite the difference between maximum depths, the measured depths coincide closely within the experimental *LED* range, as shown in Figure 4(c). Compared to the increased depth, the measured width increases more moderately as pre-alloyed widths range from 99 µm to 151 µm (Figure 4(d)), and in-situ alloyed with a range from 91 µm to 140 µm (Figure 4(e)). In the whole *LED* range, pre-alloyed meltpools are overall 9 % wider than in-situ alloyed meltpools, as shown in Figure 4(f). Width-to-depth ratios (*W*/*D*) of single-track meltpools are plotted in Figure 4(c) as well. Most of them are smaller than 1.5, indicating the meltpools are no longer operated in conduction mode within the current processing window [26].

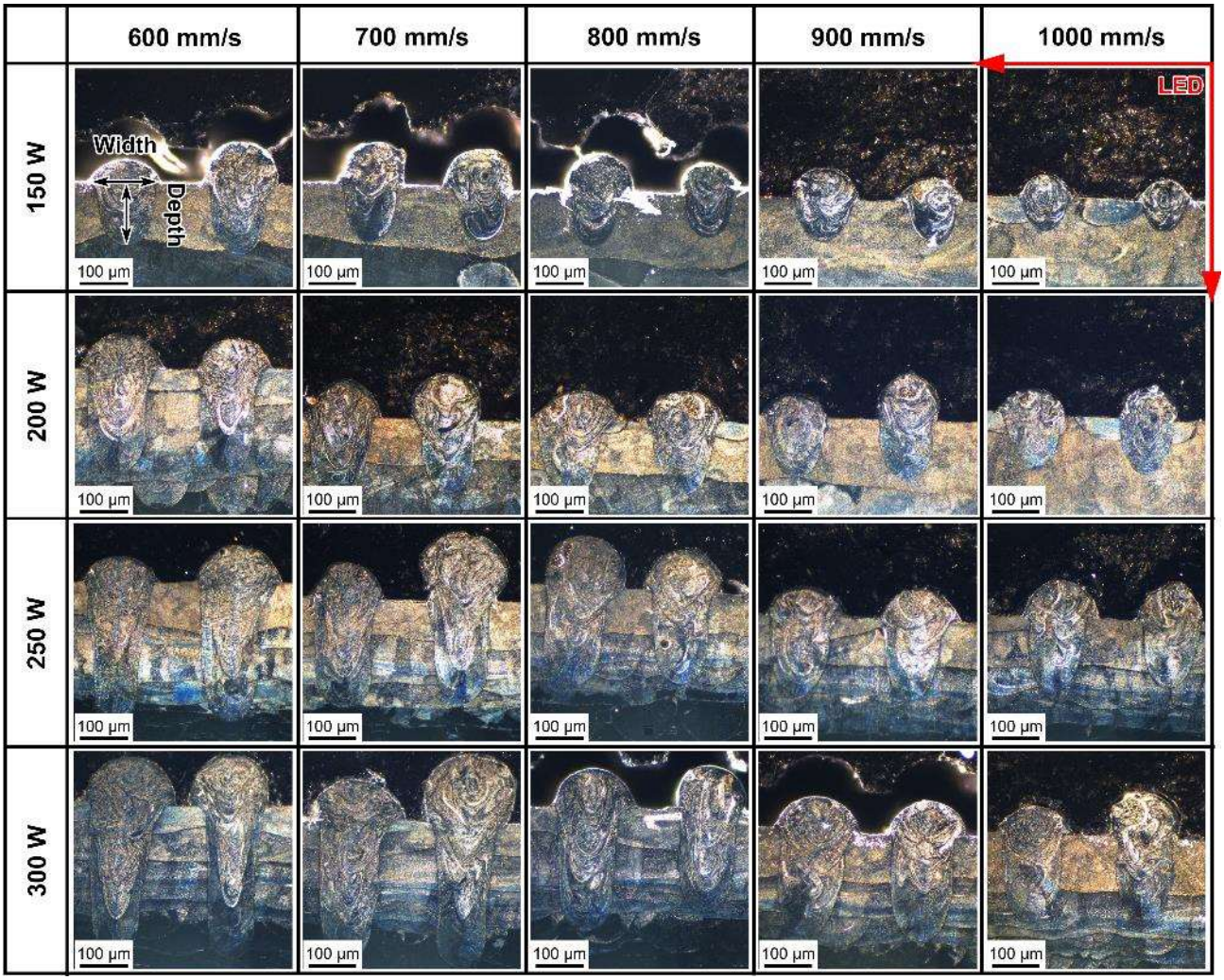

Figure 3. OM images of the single-track cross-sections, with an illustration of measuring meltpool dimensions.

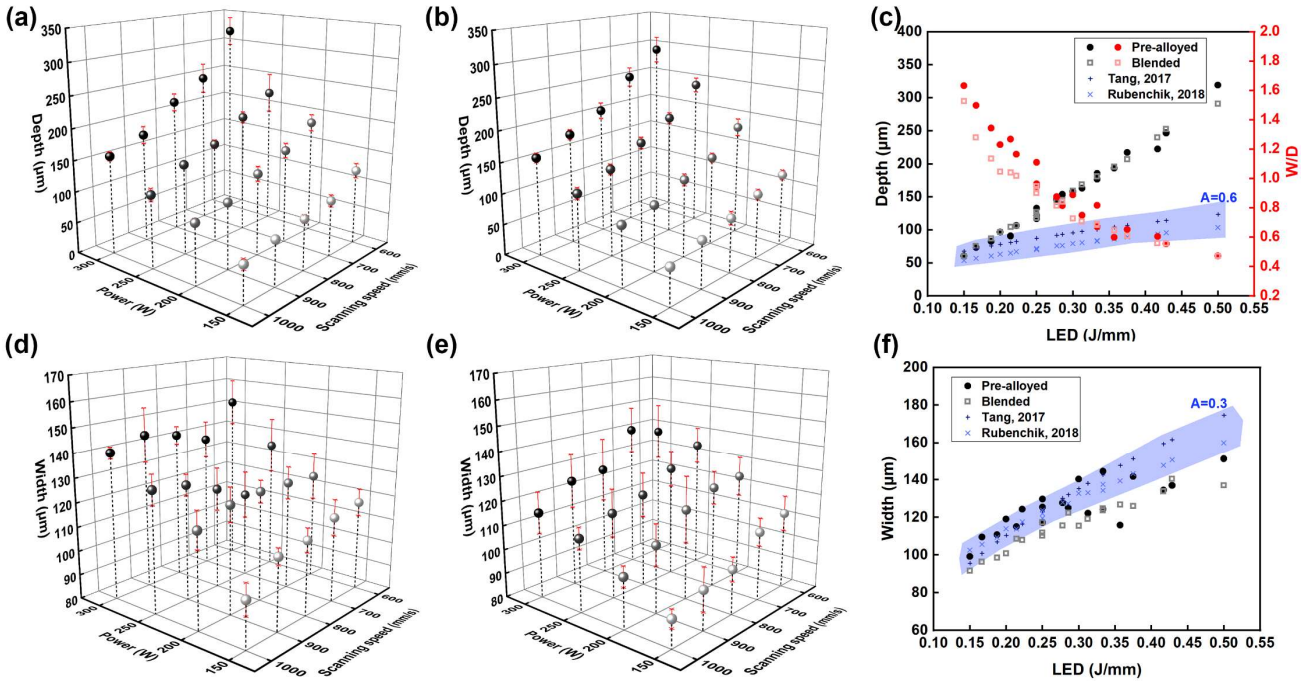

Figure 4. Measured depths of (a) pre-alloyed CoCrFeNi meltpools and (b) in-situ alloyed CoCrFeMnNi meltpools. (c) Dependence of measured and predicted depths, as well as width-to-depth ratio on linear energy density. Measured widths of (d) pre-alloyed meltpools and (e) in-situ alloyed meltpools. (f) Dependence of measured and predicted widths on linear energy density.

The predicted depths and widths of pre-alloyed meltpools using conduction-based methods are given in Figure 4(c) and (f), respectively. In Figure 4 (c), predicted results are close to measured results at low *LED* of 0.15 J/mm, which is about the threshold of conduction mode (W/D = 1.5). Then the predicted results deviate from measured depth as the *LED* increases. Both conduction-based methods predict in a similar range but tend to underestimate the depth as meltpools exceed the conduction-mode threshold. The deviation indicates that the development of meltpool depth is no longer dominated by the conduction model. Hence, methods based on conduction are not applicable at such high *LED*. On the other hand, the predicted widths seem to match experimental widths in this range, as shown in Figure 4(f). However, it must be noticed that the absorptivity for width prediction is set as 0.3, which

is normally a value for conduction meltpools and much lower than actual absorptivity (=0.6-0.8) for keyhole meltpools.

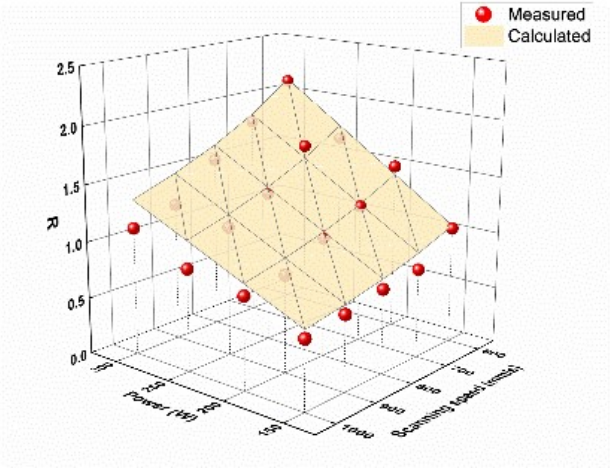

Figure 5. The comparison of aspect ratio (*R*) between measured results of pre-alloyed meltpools and predicted results calculated by the keyhole-based method (Fabbro).

On the other hand, aspect ratios calculated via the keyhole-based method are presented in Figure 5. For the printing parameters involved in this study, it shows good correspondence with experimental results, especially at high *LED*. The shape of the keyhole is more coincident with the ideally cylindrical keyhole hypothesised in this method at high *LED*, while the concave depressed by recoil pressure is relatively shallow when the meltpool is close to conduction mode. The approaches to predict the meltpool dimensions in this study have shown the importance of distinguishing meltpool modes in a given processing window. However, it is hard to determine the keyhole threshold for a particular material without practical observation on meltpools. Further analyses of keyhole formation and the applicability of modelling methods are given in discussion.

3.2. In-situ homogenisation of Mn

Figure 6 shows the distribution of Mn and pre-alloyed elements in single tracks fabricated with *LED* of 0.25, 0.5, and 0.3 J/mm, respectively. In the previous in-situ alloying study on bulk CoCrFeMnNi

HEA [24], Mn tends to be better homogenised in samples fabricated with high volumetric energy density (*VED*, defined by *P*/*vht* [8]). Good homogeneity has been achieved using *VED* of 259.3 J/mm^3, and the corresponding *LED* is 0.35 J/mm. In the present study, however, Mn shows poor homogeneity in all single tracks, although the *LED* of 0.5 J/mm adopted has exceeded that used in the homogeneous bulk sample. The distribution of Mn is also different in individual cross-sections fabricated using the same parameters, indicating heterogeneity along the scanning direction. One thing in common is that the tops of meltpools are mostly richer in Mn. In single-track experiments, the blended powder was spread on the top of pre-alloyed beds, and therefore the diffusion of Mn began from the top; meanwhile, Mn also tended to concentrate and evaporate at the surface due to the high temperature in keyhole mode. The single-track mapping results indicate that the in-situ alloyed Mn can hardly get homogenised by a single-track meltpool, even with excessive energy input.

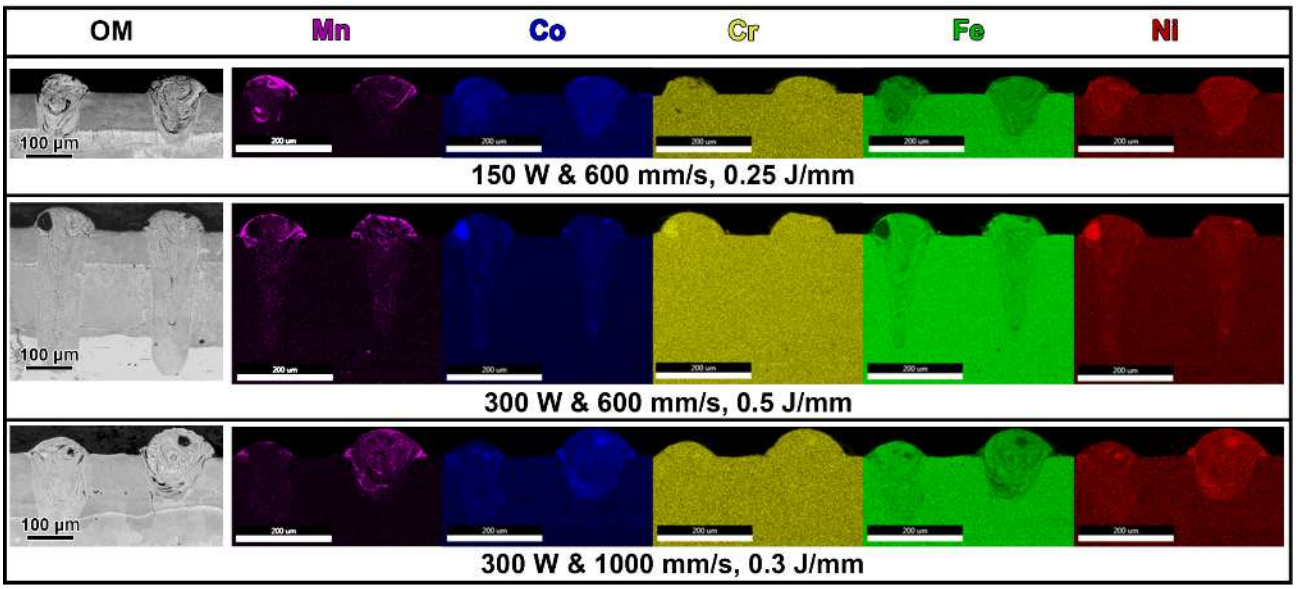

Figure 6. EDS mapping results of single tracks labelled by (*P* & *v*, *LED*).

In single layers, hatching is conducted, and therefore every track is partially remelted by its next track. Mn mapping results of representative single layers are provided in Figure 7(a). Besides Mn enrichment near the tops, which is consistent with the single-track meltpools, Mn is also slightly richer in the first track of each layer, because the first track of a layer absorbs abundant powder whereas it can only be

remelted on one side. As the scanning proceeds, the Mn in samples with hatch spacing of 60 μm shows better homogeneity. Meanwhile, Mn is also better homogenised in samples fabricated with laser power of 300 W. Previous results on meltpool dimensions have shown that meltpool width can be enlarged with high *LED*. Since the combination of a small hatch spacing and a large meltpool width results in more overlapping, single-layer mapping results indicate that sufficient remelting is critical for homogenisation of the in-situ alloy element. To further reveal the effects of inter-layer remelting, mapping results of three-layer samples are shown in Figure 7(b). Two times of inter-layer remelting are introduced by three-layer printing aside from inter-track remelting in single layers. The inner parts of three-layer samples possess significantly improved homogeneity compared to that in single layers.

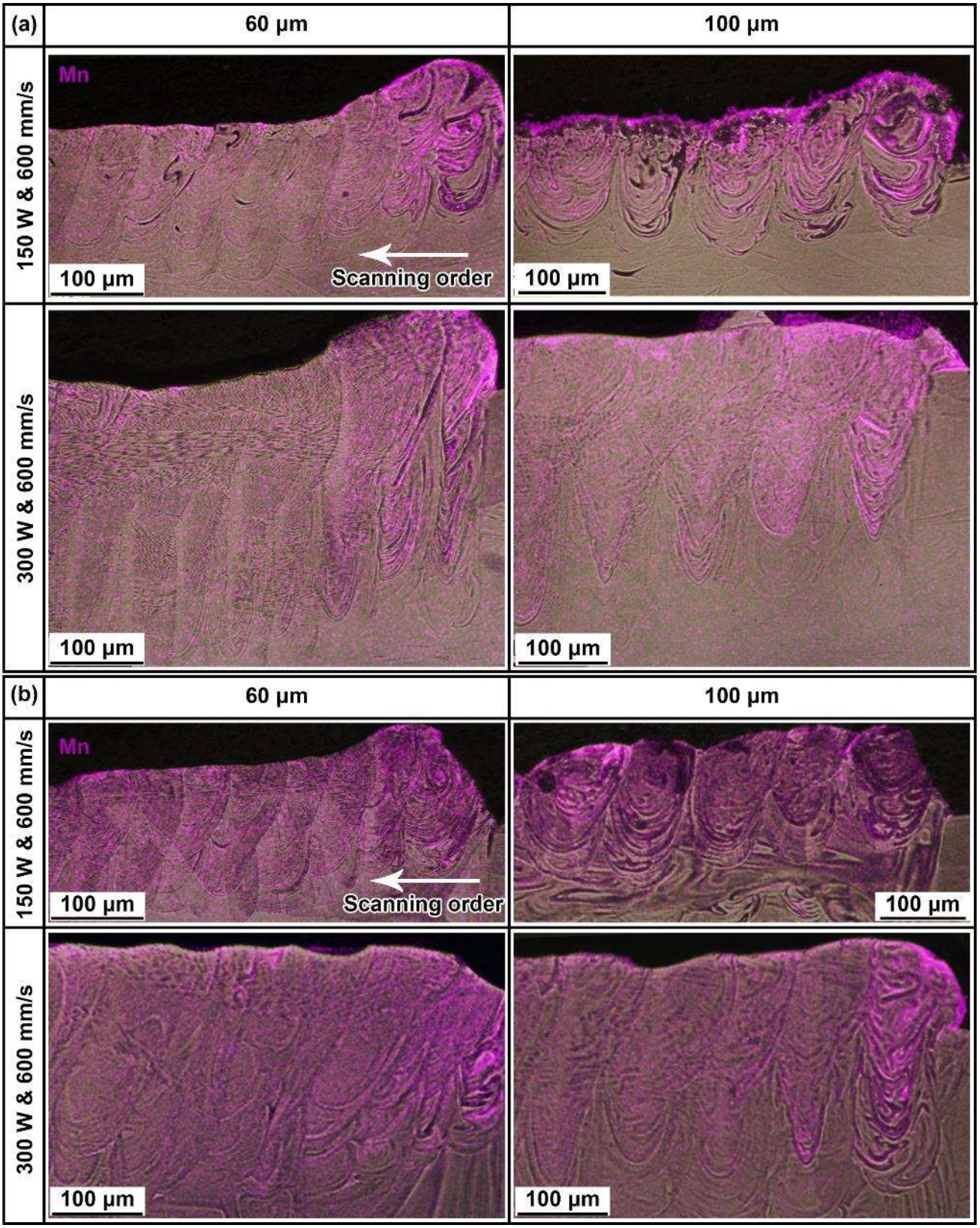

Figure 7. EDS mapping results of Mn in (a) single layers and (3) three-layer samples.

3.3. Grain development

The grain development in the LPBF process is revealed via EBSD. Figure 8 gives inverse pole figure (IPF) mapping results of single tracks built with identical *LED* of 0.25 J/mm, and two cross-sections with opposite scanning directions are included for each parameter. Meltpool boundaries in the mapping results and measured dimensions illustrate these meltpools are similar in size. The results show that most grains can grow continuously across meltpool boundaries rather than nucleation at the boundaries [43]. The epitaxial growth starts from peripheries and finally converges at midlines of meltpools after solidification. Although chemical heterogeneity is induced by in-situ alloying, grain development possesses good consistency from pre-alloyed beds to in-situ alloyed tracks. Apart from the similarity in size, preferred orientations along the scanning direction change with different laser parameters. <001> is the dominant orientation with a scanning speed of 600 mm/s, while <101> tends to take advantage as the scanning speed increases to 1000 mm/s.

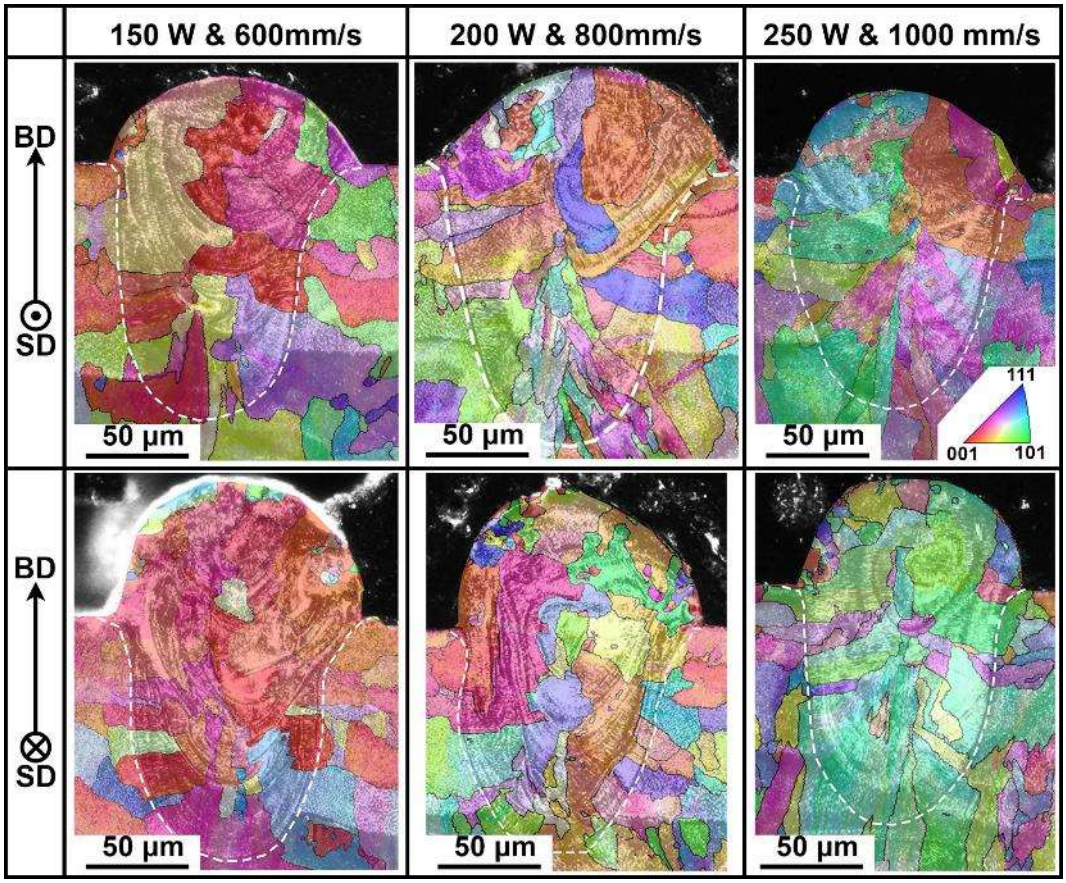

Figure 8. IPF mapping results of in-situ alloyed meltpools built with identical *LED* of 0.25 J/mm.

Further EBSD results of three-layer samples show that preferred orientations in single tracks can be inherited. The intensity of <101> is significantly more substantial in the sample fabricated using a scanning speed of 1000 mm/s, as shown by IPFs in Figure 9. Grain morphology also changes dramatically with laser parameters. In samples fabricated using 150 W & 600 mm/s, grains are separated by regular vertical boundaries parallel to the building direction. Meanwhile, the grains in samples fabricated using 250 W & 1000 mm/s tend to be randomly distributed without apparent patterns along the building direction. In those samples fabricated with hatch spacing of 60 μm, some grains can grow over 100 μm along the transverse direction. Grain size (d_{avg}) has been measured from the six representative samples and correlated to laser parameters and hatch spacing. Samples fabricated of 150 W & 600 mm/s possess the finest grain size, about 55 μm. By applying the parameter of 300 W & 600 mm/s that can enlarge meltpools, or 250 W & 1000 mm/s with a <101> preference, grains in three-layer samples are coarsened significantly. Other than laser parameters, grain size is also affected by hatch spacing as those in samples fabricated using hatch spacing of 60 μm is overall larger than those in samples with hatch spacing of 100 μm.

By comparing the grain structures from single-track samples to three-layer samples, the inheritance of preferred orientation and grain growth in the LPBF process are revealed. The correlations between grain development and parameters will be further discussed in this article.

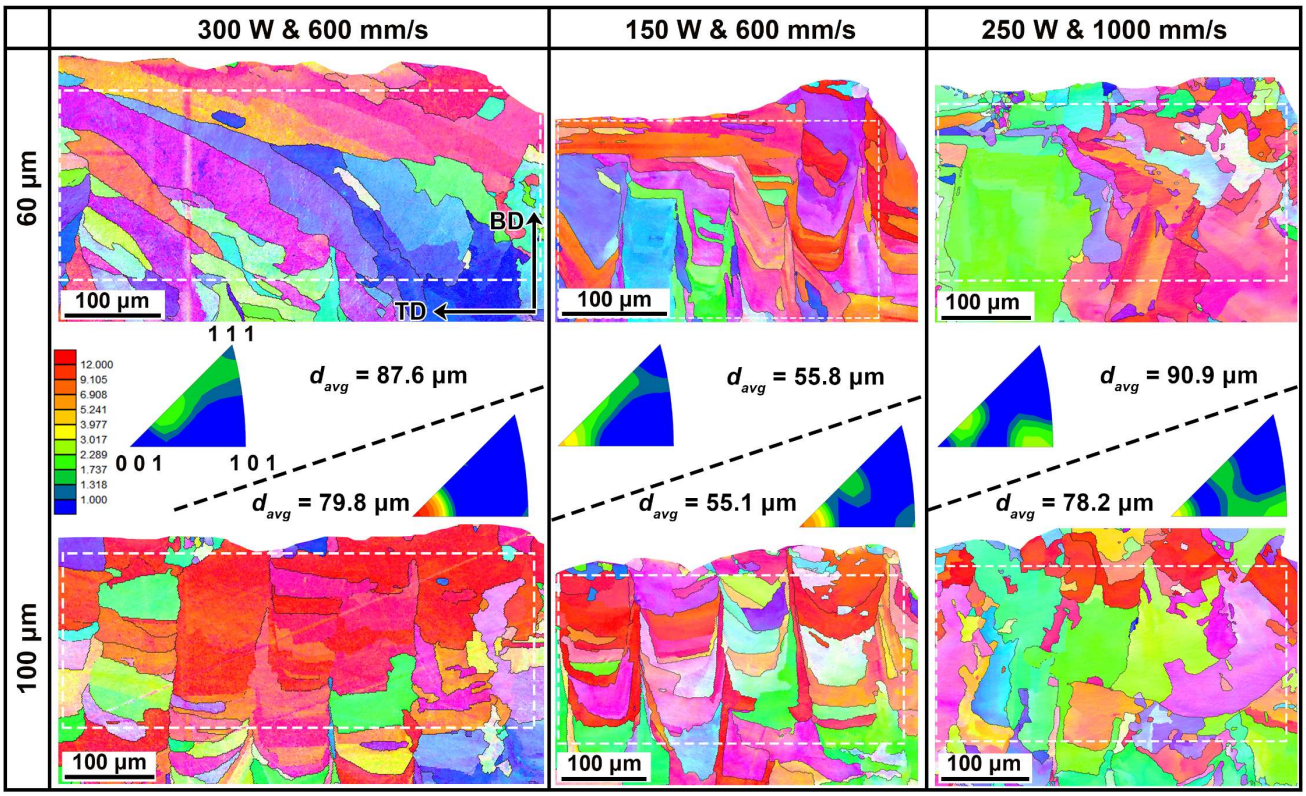

Figure 9. IPF mapping results of three-layer samples, with embedded IPFs and average grain size calculated from areas marked by dashed rectangles.

4. Discussion

4.1. The development of keyhole meltpools

4.1.1. Meltpool dimensions

Figure 10(a) illustrates the cross-section of an ideal conduction meltpool, which has not been depressed by recoil pressure on its surface and maintains a semi-circle envelope. The meltpool surface is relatively stable, and its laser absorptivity is about 0.3 for metals. Various conduction methods have shown good applicability for this type of meltpools, and the precision can be improved via further inviting modification such as introducing temperature dependence, convection consumption, gaussian-profiled laser beam, etc. [29]. However, the structure of meltpools will change dramatically and become more complex due to keyhole formation [28]. Figure 10(b) presents a schematic of a

meltpool with a deep keyhole to illustrate features of keyhole meltpools. In the keyhole mode, the surface of the meltpool is depressed by recoil pressure and results in a cavity inside the meltpool. Therefore, the expansion of meltpool is no longer a semi-circle like the conduction mode. Because the incident laser penetrates into the keyhole and reflects several times on its inner surface, the absorptivity in the keyhole mode can increase sharply from 0.3 to a range of 0.6-0.8 [39]. The conduction methods can provide an approximate trend for keyhole meltpool width with an absorptivity of conduction meltpools (e.g., 0.3), as shown in Figure 4(f). By applying an absorptivity of keyhole meltpools (e.g., 0.6), meltpool width will be overestimated by models in conduction methods. Because the meltpool boundary predicted by such conduction methods is based on a thermal field heated at the centre of the surface. Meanwhile, in a keyhole meltpool, the development of width can be considered as a heat source with a similar size of the laser beam working at the boiling point of materials. Hence, the development of width is still an approximation to the models of a conduction meltpool. The modification of absorptivity suggests that a large portion of heat input is consumed in the vertical direction due to the formation of keyhole, leading to meltpool depth deeper than the prediction by conduction methods, as illustrated in Figure 10(b).

The in-situ alloyed meltpools are overall narrower than the pre-alloyed meltpools, which might be attributed to the burning loss of Mn. As most single tracks are operated in the keyhole mode, the vaporisation of Mn is inevitable, especially at high energy density due to its lowest heat of vaporisation and lowest boiling point among the five elements. Although the quantification of Mn burning loss is hard to evaluate in single tracks, it has been noticed that the concentration of Mn could drop from 21.53 at. % to 16.67 at. % during the in-situ alloying of CoCrFeMnNi bulk samples [24]. The heat consumed by solid-liquid phase change is less than 10 % of the total heat input used to generate the entire thermal field in the scanning process [28], whereas the heat consumed by burning loss could be significant since the heat of vaporisation is many times of the heat of fusion. On the other hand, the

reduction only occurs in width while the depth is overall coincident. According to EDS results, the Mn in meltpools is brought into meltpools from the blended powder covering on pre-alloyed layers and mainly distributes in the upper part of meltpools. It suggests the heat taken away by Mn vaporisation is mainly from the upper bead of meltpools, where the width was measured. However, the rest part of meltpool especially the lower part is still dominated by pre-alloyed layers, and therefore the development of depth is mostly identical with pre-alloyed meltpools.

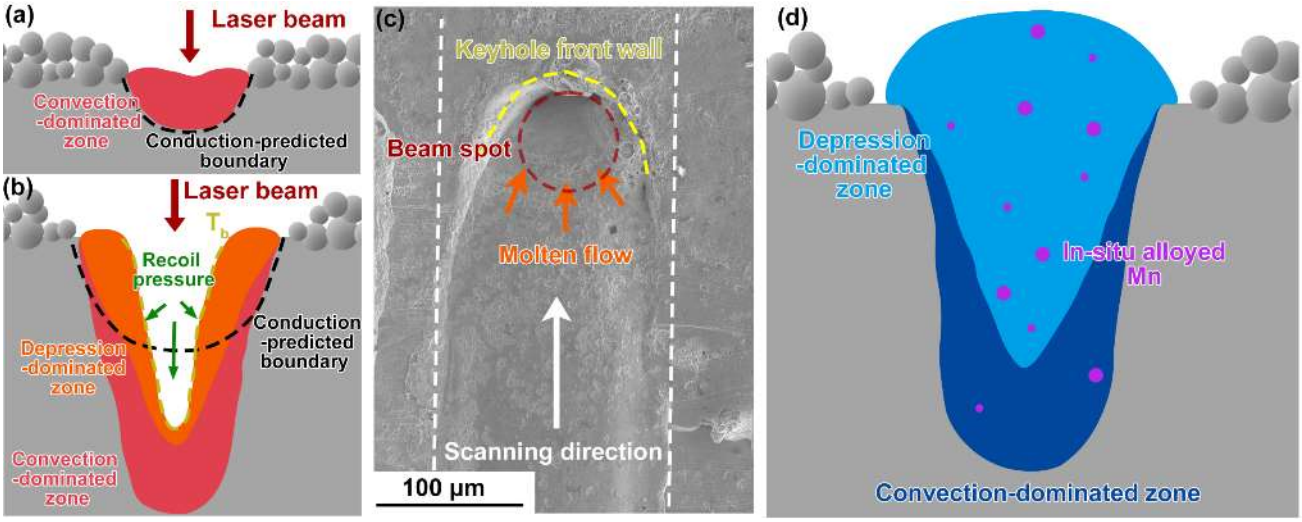

Figure 10. Schematics of (a) conduction meltpools and (b) keyhole meltpools. (c) An SEM top view at the end of a single-track sample scanned by 300 W & 600 mm/s. (d) Schematic of a solidified in-situ alloyed meltpool.

4.1.2. Elemental distribution

Apart from the dimensions, the fluid dynamics in meltpools are also changed dramatically due to the occurrence of keyhole. Figure 10(c) shows a top view at the end of a single-track meltpool, which reflects the structure of a moving keyhole meltpool. The keyhole front wall is a smooth curve, and its arc fits well with the beam spot with a diameter of 67 μm. In the scanning process, molten metal is pushed by the recoil pressure to the bottom and two flanks of the meltpool and then surges back into the cavity as the beam moves forward. The recoil pressure is orders of magnitude larger than both capillary force and thermocapillary force, the two main driven forces of flows in conduction meltpools

[44]. As illustrated in Figure 10(b), in the zone (marked as depression-dominated zone) close to the keyhole, the flow driven by the recoil pressure overrides the flows (e.g., Marangoni flow) driven by convection; meanwhile, the rest (marked as convection-dominated zone) is still mainly affected by convection. Hence, delimitation of elemental distribution occurs in the keyhole meltpool due to two flow patterns. As mentioned before, the blended powder is brought into an in-situ alloying meltpool downward, indicating Mn would primarily distribute in the depression-dominated zone but rarely spread to the convection-dominated zone, as shown in Figure 10(d).

Figure 11(a) provides two cross-sections of keyhole meltpools. The delimitation of flows can be inherited after solidification and revealed by etching. Despite meltpool boundaries and the flow delimitation, the HEA grains can grow continuously through them during rapid solidification. On the other hand, the homogenisation of Mn is separated by the delimitation, as shown in Figure 11(b). Mn from the blended powder is mainly distributed in the depression-dominated zone, but the heterogeneity of Mn does not break the epitaxial growth of grains. The in-situ alloyed Mn reveals that the flows with disparate intensity co-exist in the keyhole meltpool. Once the depression-dominated zone occurs, it overrides convection-dominated zone in terms of in-situ homogenisation. This phenomenon indicates that applying keyhole meltpools in LPBF in-situ alloying is helpful to the homogenisation of added elements or particles.

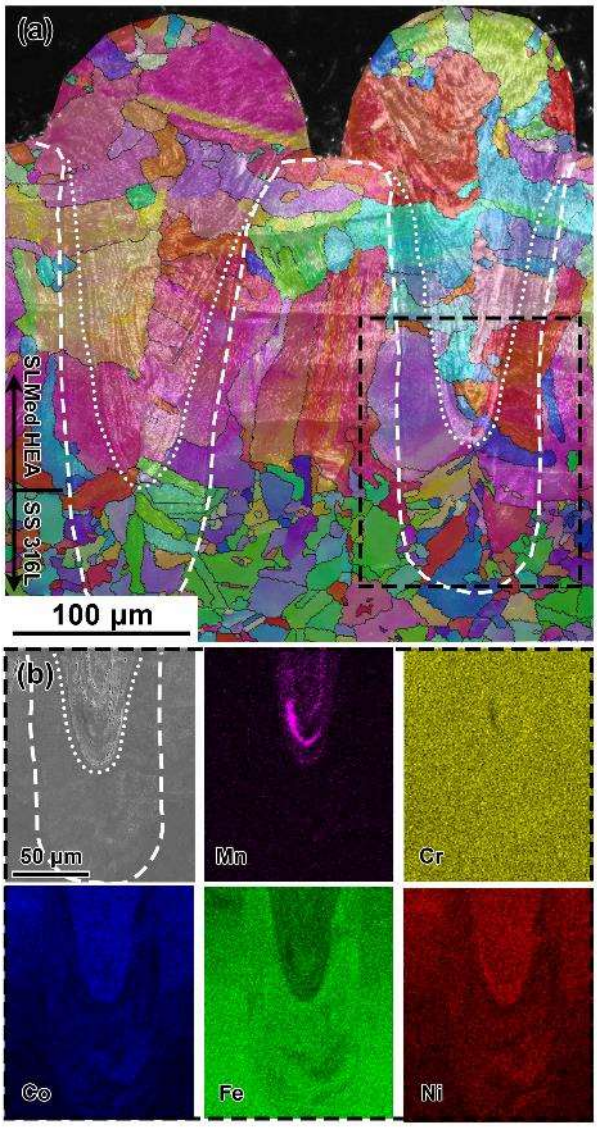

Figure 11. (a) IPF mapping & OM results of in-situ alloyed meltpools scanned by 300 W & 600 mm/s, and (b) EDS mapping results of the area marked by the black dashed line. White dashed lines and dotted lines mark the meltpool boundary and internal delimitation, respectively.

4.2. In-situ alloying homogenisation in the LPBF process

In the LPBF process, single tracks will interact with each other. Remelting is also important to the final quality of LPBFed parts.

For in-situ alloying, even by operating in keyhole mode that introduces intensive flow, single tracks

cannot achieve ideal homogeneity, whereas similar laser parameters could produce good homogeneity in the bulk samples [24]. Zhang et al. [19] have reported that the atomic diffusion in meltpools is restricted by the short existing duration, and hence its contribution to homogenisation is also not significant. It suggests remelting is the critical factor for in-situ homogenisation in the LPBF process. Figure 12 provides EDS line scanning results of single layers to assess the effect of inter-track remelting. Figure 12(a) shows that the Mn is barely homogenised in the sample 150 W & 600 mm/s since the hatch spacing is close to its meltpool width (111.8 μm), indicating most of the meltpool has not been remelted during the single-layer printing. The homogenisation is significantly improved with the same laser parameters when hatch spacing is set as 60 μm, as shown in Figure 12(b). For a given combination of meltpool width and hatch spacing, the horizontal melting cycle M_h can be estimated by $M_h=W/h$. So the M_h is improved from 1.12 to1.86 as the hatch spacing decreases from 100 μm to 60 μm. On the other hand, the meltpool width increases to 136.9 μm with higher laser power 300 W; hence the M_h using the same hatch spacing can be improved as well.

Inter-layer remelting can be estimated according to given layer thickness and meltpool depth. The in-situ alloying meltpool depth of 300 W & 600 mm/s is ~290 μm, much deeper than the layer thickness of 30 μm. Therefore, the vertical melting cycle (M_v) experienced by each layer is about 9.67 (given by D/t [21]). For a bulk sample built by LPBF, the total melting cycle is given by $M_hM_v=WD/\mathrm{ht}$. A large remelting cycle indicates the material solidified previously could be remelted more times in the LPBF process, leading to improvement of the overall homogenisation. The in-situ homogenisation of Mn in bulk samples has been revealed to be positively correlated to the volumetric energy density [24]. Since the *VED* can also be expressed by *LED*/*ht*, both width and depth are positively correlated to the *LED*, as shown in Figure 4(c) and (f). The expression of *VED* reflects the melting cycle as well, where *P* and *v* stand for meltpool size, while *h* and *t* stand for the density of scanning routes. The melting cycle experienced by the bulk samples with good homogeneity is estimated to be 16.8

according to its parameters which produce the *VED* of 259.3 J/mm^3. It explains the trend that Mn is better homogenised in bulk samples fabricated with high *VED*.

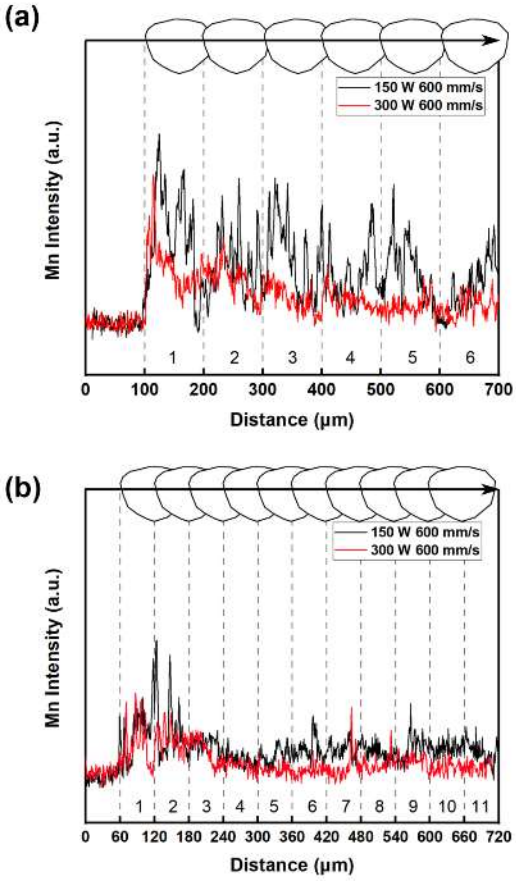

Figure 12. EDS line scanning results of Mn in single layers fabricated with hatch spacing of (a) 100 μm, and (b) 60 μm. The scanning lines are drawn 30 μm beneath the surfaces of layers. The arrows in figures mark the scanning consequences of tracks in layers.

4.3. Grain development in the LPBF process

4.3.1. Horizontal grain coarsening

The grain development is correlated to remelting as well. Figure 13(a) shows a single layer with coarsened grains growing through multiple meltpools in the transverse direction. Such horizontal growth is abundant in three-layer samples with a small hatch spacing of 60 μm, as shown in Figure 9, indicating those bulk samples fabricated using small hatch spacing could inherit the coarse

microstructures. Figure 13(b) illustrates the mechanism of horizontal growth affected by remelting in a layer. Firstly, in a single-track meltpool, grains grow from the boundary to the midline direction during solidification. Two different scenarios could occur: (a) For the hatch spacing larger than half width of the meltpool, only the grains on the remelted side in the first track can grow continuously into the next track, while the grains on the other side keep their boundaries along the vertical midline. As the scanning continues, such vertical midlines are repeated and separate the layer into grains whose widths approximate the hatch spacing [43, 45]. (b) For a hatch spacing smaller than half width, the midlines can be remelted by the second track. Growth in this situation is not interrupted by the midlines and can continue in the transverse direction, resulting in abnormally large grains, similar to, e.g., the three-layer sample printed using 300 W & 600 mm/s in Figure 9. Because meltpools are wide at the top, grain coarsening is mainly observed near the top of a layer, as shown in Figure 13(a). This phenomenon can help tailor the grain size in horizontal directions for materials with a wide processing window. Nevertheless, assuming the epitaxial growth in single tracks is dominated by nucleation, the microstructures could be refined by applying small hatch spacing since the density of meltpool boundaries is increased by this way.

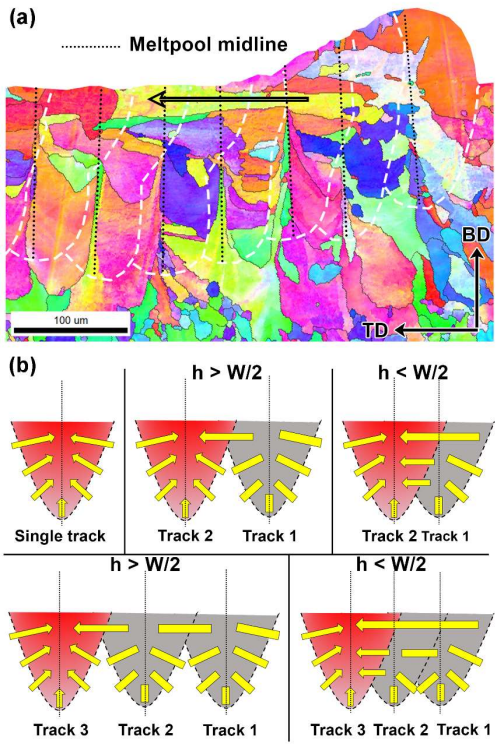

Figure 13. (a) IPF mapping of the single-layer sample fabricated with 150 W & 600 mm/s and hatch spacing of 60 µm. (b) A schematic of horizontal grain growth with different hatch spacings. Yellow arrows represent the growing direction of grains.

4.3.2. Texture inheritance

Texture is an important factor for the performance of LPBFed parts. Several reports have shown that the texture in LPBFed parts can be tailored via processing optimisation without changing powder or printer [46, 47]. This study shows that the preferred grain orientations of LPBFed parts vary in single tracks and can be progressively inherited during the layer-by-layer process. So, to tailor the texture in bulk samples, texture development in single tracks can be an important starting point.

The cross-sections provided in Figure 8 are similar in their dimensions as solidified single tracks. Meanwhile, during the laser scanning process, the meltpool length is mainly correlated to the scanning speed [29, 42]. The meltpools formed by scanning speed of 1000 mm/s are longer than those printed

by scanning speed of 600 mm/s. Combinations of similar depth but different lengths could lead to different slopes at the rear wall of meltpools. And since the solidification takes place at the meltpools rear wall in the LPBF process, the grain development is also affected. Considering a short meltpool that is nearly movement-free, its rear wall is nearly perpendicular to the scanning direction, and therefore the direction of the local thermal gradient (G) at its rear wall is almost antiparallel to its scanning direction [43]. As the scanning speed increases, the meltpool is stretched in the scanning direction, and the direction of G starts to change from the scanning direction to the vertical direction. For the fcc HEAs in this study, <001> is the preferred growing direction that aligned with the direction of G, and therefore the growth of <001> should change from scanning direction to vertical direction as well, leading to the change of corresponding crystallography orientations in the scanning direction. The texture in single tracks also influences the grain morphology in three-layer samples. The regular vertical boundaries disappear as the preferred orientation in single tracks changes from <001> to <101>, leading to coarsening of grains, as shown in Figure 9. Since the occurrence of such boundaries is due to the convergence of grain growth from different directions in the transverse plane, it indicates that the overall G alignment between adjacent tracks is somehow improved in the <101>-preferred meltpool. By manipulating the crystallography and the associated G patterns in the whole LPBF process, it is possible to achieve the customisability of grain structures in the future.

4.4. Defects accumulated in the LPBF process

In this study, the LPBF building process is conducted up to three layers; some defects that may occur in bulk samples can be predicted by analysing three-layer samples.

Figure 14(a) shows a three-layer sample in which the tracks barely overlap with each other. In this situation, the meltpool width is close to or even smaller than the hatch spacing. Although there is no apparent gap between these tracks in this cross-section, such insufficient hatching can lead to

lack-of-fusion pores as multiple layers pile up. Bulk samples produced using corresponding *VED* (50 J/mm^3) are poorly densified due to abundant lack-of-fusion pores [8, 24].

As mentioned in previous sections, the meltpools in this study are mostly operated in the keyhole mode. However, keyhole pores are rarely observed inside those meltpools. It is discussed as follows: The primary pore-forming mechanism under the keyhole mode is that the molten flow from the keyhole rear wall reaches the front wall, resulting in collapse at the keyhole bottom during laser movement. However, once the scanning speed is fast enough to keep a stable distance between the rear and front walls, collapse can be avoided in keyhole meltpools. Keyhole meltpools with stable and open depression zone have also been observed by Guo et al. and Kouraytem et al. [42, 44] in their in-situ study and with scanning speed beyond 600 mm/s. Hence the keyhole mode is not identical to a pore trigger. On the other hand, keyhole pores are frequently observed at the edge of the three-layer samples, as shown in Figure 14(b). The location of these pores is much deeper than the meltpool depth measured from corresponding single tracks, implying that they are hard to be eliminated by remelting. The formation of such pores is due to the acceleration and deacceleration of the laser at the ends of tracks. Especially for high laser power, the beam spot can be held for too long before its move to next point, leaving a meltpool that much deeper than the stable meltpool in the rest of the track. Even with moderate *LED* that theoretically generates a conduction meltpool, keyhole pores may still occur at the boundary of a layer, where tracks start and end. Considering the edge-area keyhole pores, shift and rotation can be set between layers to avoid such defects from concentrating locally in LPBFed parts. Moreover, to further improve the densification, it is worth optimising the acceleration and deacceleration process as well [21].

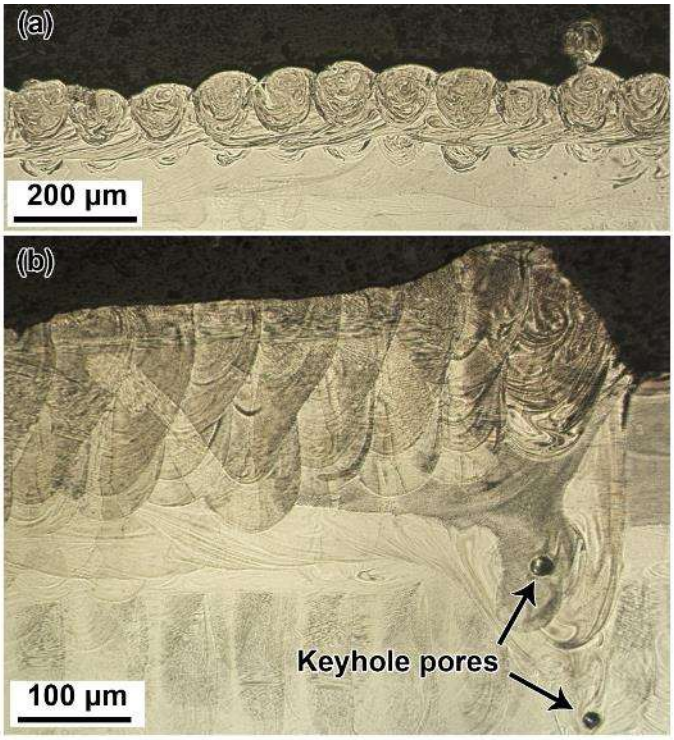

Figure 14. OM images of (a) a three-layer sample without good hatching and (b) a three-layer sample with keyhole pores at its edge.

5. Conclusions

By tracing the LPBF in-situ alloying process back to single tracks, the microstructural evolution and its correlation to printing parameters are revealed in terms of meltpool dimensions, elemental homogenisation, and grain development. The key findings are summarised as below:

(1) In the *LED* range between 0.15 J/mm and 0.5 J/mm, meltpools are no longer in the conduction mode and they start to work in the keyhole mode. The comparison between modelling methods suggests their applicability further depending on the meltpool modes. The addition of elemental Mn powder led to 9 % decrease of meltpool widths, whereas meltpool depths maintained similarly in the *LED* range.

(2) The intense flow generated in the keyhole meltpool dominates the homogenisation of Mn due to its superior intensity. Remelting is also a critical factor to achieve homogeneity in the LPBF

process, and the total melting cycle can be higher than 10 in a well-homogenised part.

(3) Correlations between grain structures and printing parameters are evaluated from the scope of single tracks. Using hatch spacing smaller than half width of meltpool promotes the horizontal grain growth. The texture in LPBF parts reflects the inheritance of preferred orientations from single tracks. Moreover, the preferred orientations in single tracks can be tailored by adjusting laser power and scanning speed.

Acknowledgements

This research was supported by Research and Development Program Project in Key Areas of Guangdong Province [grant number 2019B090907001], Shenzhen Science and Technology Innovation Commission [grant number JCYJ20180504165824643 and JCYJ20170817111811303], and the National Natural Science Foundation of China [grant numbers 51971108, U19A2085].

References

[1] Brif Y, Thomas M, Todd I. The use of high-entropy alloys in additive manufacturing [J]. Scr. Mater., 2015, 99 93

[2] Joseph J, Jarvis T, Wu X, et al. Comparative study of the microstructures and mechanical properties of direct laser fabricated and arc-melted AlxCoCrFeNi high entropy alloys [J]. Mater. Sci. Eng., A, 2015, 633 184

[3] Li X. Additive Manufacturing of Advanced Multi-Component Alloys: Bulk Metallic Glasses and High Entropy Alloys [J]. Adv. Eng. Mater., 2017, 1700874

[4] Kim J, Wakai A, Moridi A. Materials and manufacturing renaissance: Additive manufacturing of high-entropy alloys [J]. J. Mater. Res., 2020, 35(15): 1963

[5] Zhou P F, Xiao D H, Wu Z, et al. Al0.5FeCoCrNi high entropy alloy prepared by selective laser melting with gas-atomized pre-alloy powders [J]. Mater. Sci. Eng., A, 2019, 739 86

[6] Han C, Fang Q, Shi Y, et al. Recent Advances on High-Entropy Alloys for 3D Printing [J]. Adv Mater, 2020,

[7] Lin D, Xu L, Jing H, et al. Effects of annealing on the structure and mechanical properties of FeCoCrNi high-entropy alloy fabricated via selective laser melting [J]. Addit. Manuf., 2020, 32 101058

[8] Li R, Niu P, Yuan T, et al. Selective laser melting of an equiatomic CoCrFeMnNi high-entropy alloy: Processability, non-equilibrium microstructure and mechanical property [J]. J. Alloys Compd., 2018, 746 125

[9] Kim Y-K, Choe J, Lee K-A. Selective laser melted equiatomic CoCrFeMnNi high-entropy alloy: Microstructure, anisotropic mechanical response, and multiple strengthening mechanism [J]. J. Alloys Compd., 2019, 805 680

[10] Piglione A, Dovgyy B, Liu C, et al. Printability and microstructure of the CoCrFeMnNi high-entropy alloy fabricated by laser powder bed fusion [J]. Mater. Lett., 2018, 224 22

[11] Ren J, Mahajan C, Liu L, et al. Corrosion Behavior of Selectively Laser Melted CoCrFeMnNi High Entropy Alloy [J]. Metals, 2019, 9(10): 1029

[12] Park J M, Choe J, Kim J G, et al. Superior tensile properties of 1%C-CoCrFeMnNi high-entropy alloy additively manufactured by selective laser melting [J]. Mater. Res. Lett., 2019, 1

[13] Li B, Qian B, Xu Y, et al. Fine-structured CoCrFeNiMn high-entropy alloy matrix composite with 12 wt% TiN particle reinforcements via selective laser melting assisted additive manufacturing [J]. Mater. Lett., 2019, 252 88

[14] Jodi D E, Park J, Park N. Strengthening of ultrafine-grained equiatomic CoCrFeMnNi high-entropy alloy by nitrogen addition [J]. Mater. Lett., 2020, 258 126772

[15] Zhang Y, Zuo T T, Tang Z, et al. Microstructures and properties of high-entropy alloys [J]. Prog. Mater. Sci., 2014, 61 1

[16] DebRoy T, Wei H L, Zuback J S, et al. Additive manufacturing of metallic components – Process, structure and properties [J]. Prog. Mater. Sci., 2018, 92 112

[17] Dong Y, Li Y, Ebel T, et al. Cost-affordable, high-performance Ti–TiB composite for selective laser melting additive manufacturing [J]. J. Mater. Res., 2020, 1

[18] Mosallanejad M H, Niroumand B, Aversa A, et al. In-situ alloying in laser-based additive manufacturing processes: A critical review [J]. J. Alloys Compd., 2021, 872 159567

[19] Zhang Z H, Zhou Y H, Zhou S Y, et al. Mechanically Blended Al: Simple but Effective Approach to Improving Mechanical Property and Thermal Stability of Selective Laser-Melted Inconel 718 [J]. Metallurgical and Materials Transactions a-Physical Metallurgy and Materials Science, 2019, 50a(8):

[20] Zhang B, Fenineche N-E, Liao H, et al. Microstructure and Magnetic Properties of Fe–Ni Alloy Fabricated by Selective Laser Melting Fe/Ni Mixed Powders [J]. J. Mater. Sci. Technol., 2013, 29(8): 757

[21] Duan R, Li S, Cai B, et al. In situ alloying based laser powder bed fusion processing of β Ti–Mo alloy to fabricate functionally graded composites [J]. Composites Part B: Engineering, 2021, 222

109059

[22] Polozov I, Sufiiarov V, Popovich A, et al. Synthesis of Ti-5Al, Ti-6Al-7Nb, and Ti-22Al-25Nb alloys from elemental powders using powder-bed fusion additive manufacturing [J]. J. Alloys Compd., 2018, 763 436

[23] Popov V V, Katz-Demyanetz A, Koptyug A, et al. Selective electron beam melting of Al0.5CrMoNbTa0.5 high entropy alloys using elemental powder blend [J]. Heliyon, 2019, 5(2):

[24] Chen P, Li S, Zhou Y, et al. Fabricating CoCrFeMnNi high entropy alloy via selective laser melting in-situ alloying [J]. J. Mater. Sci. Technol., 2020, 43 40

[25] Guo C, Xu Z, Zhou Y, et al. Single-track investigation of IN738LC superalloy fabricated by laser powder bed fusion: Track morphology, bead characteristics and part quality [J]. J. Mater. Process. Technol., 2021, 290 117000

[26] Johnson L, Mahmoudi M, Zhang B, et al. Assessing printability maps in additive manufacturing of metal alloys [J]. Acta. Mater., 2019, 176 199

[27] Mukherjee T, Zuback J S, De A, et al. Printability of alloys for additive manufacturing [J]. Sci Rep, 2016, 6

[28] Fabbro R, Dal M, Peyre P, et al. Analysis and possible estimation of keyhole depths evolution, using laser operating parameters and material properties [J]. J. Laser Appl., 2018, 30(3): 032410

[29] Rubenchik A M, King W E, Wu S S. Scaling laws for the additive manufacturing [J]. J. Mater. Process. Technol., 2018, 257 234

[30] Tang M, Pistorius P C, Beuth J L. Prediction of lack-of-fusion porosity for powder bed fusion [J]. Addit. Manuf., 2017, 14 39

[31] Rosenthal D. Mathematical theory of heat distribution during welding and cutting [J]. Weld. J., 1941, 20(5):

[32] <WJ_1983_12_s346.pdf> [J].

[33] <Hann2010_Chapter_KeyholingOrConductionPredictio.pdf> [J].

[34] Fabbro R. Melt pool and keyhole behaviour analysis for deep penetration laser welding [J]. J. Phys. D: Appl. Phys., 2010, 43(44): 445501

[35] Promoppatum P, Yao S-C, Pistorius P C, et al. A Comprehensive Comparison of the Analytical and Numerical Prediction of the Thermal History and Solidification Microstructure of Inconel 718 Products Made by Laser Powder-Bed Fusion [J]. Engineering, 2017, 3(5): 685

[36] Goossens L R, Van Hooreweder B. A virtual sensing approach for monitoring melt-pool dimensions using high speed coaxial imaging during laser powder bed fusion of metals [J]. Addit. Manuf., 2021, 40 101923

[37] <1-s2.0-S2212827120311975-main.pdf> [J].

[38] Chou H-P, Chang Y-S, Chen S-K, et al. Microstructure, thermophysical and electrical properties in AlxCoCrFeNi ($0 \leqslant x \leqslant 2$) high-entropy alloys [J]. Mater. Sci. Eng., B, 2009, 163(3): 184

[39] Ye J, Khairallah S A, Rubenchik A M, et al. Energy Coupling Mechanisms and Scaling Behavior Associated with Laser Powder Bed Fusion Additive Manufacturing [J]. Adv. Eng. Mater., 2019, 21(7): 1900185

[40] Trapp J, Rubenchik A M, Guss G, et al. In situ absorptivity measurements of metallic powders during laser powder-bed fusion additive manufacturing [J]. Appl. Mater. Today, 2017, 9 341

[41] Yao H, Qiao J-W, Gao M, et al. MoNbTaV Medium-Entropy Alloy [J]. Entropy, 2016, 18(5): 189

[42] Guo Q, Zhao C, Qu M, et al. In-situ characterization and quantification of melt pool variation under constant input energy density in laser powder bed fusion additive manufacturing process [J]. Addit. Manuf., 2019, 28 600

[43] Pham M S, Dovgyy B, Hooper P A, et al. The role of side-branching in microstructure development in laser powder-bed fusion [J]. Nat Commun, 2020, 11(1):

[44] Kouraytem N, Li X, Cunningham R, et al. Effect of Laser-Matter Interaction on Molten Pool Flow and Keyhole Dynamics [J]. Phys. Rev. Appl, 2019, 11(6):

[45] Nadammal N, Cabeza S, Mishurova T, et al. Effect of hatch length on the development of microstructure, texture and residual stresses in selective laser melted superalloy Inconel 718 [J]. Mater. Des., 2017, 134 139

[46] Attard B, Cruchley S, Beetz C, et al. Microstructural control during laser powder fusion to create graded microstructure Ni-superalloy components [J]. Addit. Manuf., 2020, 36 101432

[47] Zou J, Gaber Y, Voulazeris G, et al. Controlling the grain orientation during laser powder bed fusion to tailor the magnetic characteristics in a Ni-Fe based soft magnet [J]. Acta. Mater., 2018, 158 230